Bosonic Anomalies in Boron-Doped Polycrystalline Diamond

Gufei Zhang,[1,*] Tomas Samuely,[2] Jozef Kačmarčík,[2] Evgeny A. Ekimov,[3] Jun Li,[4] Johan Vanacken,[1] Pavol Szabó,[2] Junwei Huang,[1] Paulo J. Pereira,[1] Dorin Cerbu,[1] and Victor V. Moshchalkov[1,†]

[1]*INPAC-Insititute for Nanoscale Physics and Chemistry, KU Leuven, Celestijnenlaan 200D, B-3001 Leuven, Belgium*

[2]*Centre of Low Temperature Physics, Institute of Experimental Physics, Slovak Academy of Sciences & Faculty of Science, P. J. Šafárik University, 04001 Košice, Slovakia*

[3]*Vereshchagin Institute for High Pressure Physics, Russian Academy of Sciences, 142190 Troitsk, Moscow Region, Russia*

[4]*RISE, Nanjing University, 210093 Nanjing, China*

(Received 28 June 2016; revised manuscript received 5 October 2016; published 21 December 2016)

Quantum confinement and coherence effects are considered the cause of many specific features for systems which are generally low dimensional, strongly disordered, and/or situated in the vicinity of the metal-insulator transition. Here, we report on the observation of anomalous resistance peak and specific heat peaks superimposed at the superconducting transition of heavily boron-doped polycrystalline bulk diamond, which is a three-dimensional system situated deep on the metallic side of the boron-doping-driven metal-insulator transition in diamond. The anomalous resistance peak and specific heat peaks are interpreted as a result of confinement and coherence effects in the presence of intrinsic and extrinsic granularity. Our data, obtained for superconducting diamond, provide a reference for understanding the superconductivity in other granular disordered systems. Furthermore, our study brings attention to the significant influence of granular disorder on the physical properties of boron-doped diamond, which is considered a promising candidate for electronics applications.

DOI: 10.1103/PhysRevApplied.6.064011

I. INTRODUCTION

Since the preparation of synthetic diamond by Hall at General Electric in 1954, industry has benefited more and more from this material. With a low fabrication cost, synthetic diamond brings in nearly all the unique advantages of natural diamond, e.g., the robust mechanical strength, the extraordinarily high thermal conductivity, the remarkable resistance to contamination and chemical etching, and so on. Besides its wide use in machinery and the mining industry, the applications of synthetic diamond in microelectronics and power electronics also become feasible. The combination of the high thermal conductivity, large breakdown voltage, and the tunable electronic properties upon doping makes synthetic diamond a promising candidate for 21st-century electronics [1].

In 2004, superconductivity, observed in heavily boron-doped synthetic diamond [2,3], opened additional perspectives for the potential applications of this material in an even wider range, e.g., the diamond-based superconducting quantum interference device (SQUID) and superconducting diamond tips for the local probing techniques such as scanning tunneling microscopy (STM) and scanning tunneling spectroscopy (STS) [4,5]. Since the discovery of superconductivity in diamond, two main groups of artificial diamond, CVD (chemical vapor deposition) diamond and HPHT (high-pressure high-temperature) diamond, as categorized according to their synthetic methods, have drawn considerable attention [2,3]. Although CVD diamond in the form of film is generally considered to be more promising for applications, as it can be easily shaped into superconducting devices [1,3], HPHT diamond does have its own advantages. The naturally formed sharp edges of freestanding superconducting HPHT diamond make it a straightforward candidate for local probing tips [5], which are more robust, much harder to contaminate, and can have a higher resolution than tips made of conventional materials. Such diamond tips are also useful for imprinting in micro- and nanofabrications.

In spite of the difference between their synthetic methods and forms, CVD and HPHT diamonds demonstrate very similar physical properties in many cases, e.g., the broadening of the resistive superconducting transition when the applied magnetic field is increased [6,7], the negative temperature coefficient of the normal-state resistivity, even when the boron doping level goes well above the critical doping level for the insulator-metal transition in diamond ($\sim 3 \times 10^{20}$ cm^{-3}) [2,7–12], modulations of the local superconducting order parameter [7,13], etc. The similarity between their physical properties is not simply because superconducting CVD and HPHT diamonds are the same

*Gufei.Zhang@fys.kuleuven.be
†Victor.Moshchalkov@fys.kuleuven.be

kind of material, but mostly due to their common grounds of being a doped insulator [14,15], granular disordered, and situated in the three-dimensional (3D) regime [7,11,14]. These two systems, therefore, can be used to mimic each other and other similar superconductors.

In this article, we report on our observations of anomalous resistance peak and specific heat peaks in boron-doped polycrystalline HPHT diamond. Different from the data reported before for CVD diamond films [9,16], the resistance peak observed in this work is superimposed in a two-step resistive superconducting transition. Besides the main specific heat peak observed upon the resistive superconducting transition, an additional peak is found below the offset critical temperature of the transition. The bosonic nature of these anomalous peaks, as suggested by their locations, is confirmed by our experiments in different applied magnetic fields. We interpret these peaks and the two-step superconducting transition as a result of confinement and coherence effects in the presence of granular disorder. Our data, obtained from HPHT diamond, provide a series of experimental facts applicable not only for CVD diamond but also for other granular disordered systems. Our analysis of the resistance peak can be directly used for the theoretical modeling of similar observations in other superconducting materials and devices.

II. EXPERIMENT

A. HPHT synthesis of boron-doped polycrystalline bulk diamond

Synthesis of the boron-doped polycrystalline diamond is carried out under high pressure and high temperature conditions. A graphite bar (^{12}C 99 at. %, C 99.999%) with boron (^{10}B 96 at. %, B 99.9% crystalline, Alfa Aesar) embedded in the center is placed in a HPHT chamber. Under a pressure of 8–9 GPa, the boron-graphite assembly is heated by passing an electric current through the graphite bar. As soon as the temperature in the center of the bar reaches the temperature of the eutectic melt in the B-C system (~2500 K), diamond formation takes place at the boron-graphite interface [2,7]. After synthesis, the eutectic assembly is crushed into coarse pieces to gain access to the central boron-enriched part of the material. The pieces are subsequently acid treated to remove nondiamond phases. Afterwards, the total concentration of boron in the polycrystalline diamond is estimated at a level of about 3% [7]. The acid-treated coarse pieces (about 0.9 mm in length, 0.6 mm in width, and 0.3 mm in thickness) are directly used for our experiments.

B. Electrical transport and specific heat measurements

To characterize the electrical transport properties of the so-prepared HPHT diamond, silver wires are connected to the sample by using silver paste for electrical contacts. Four-terminal ac measurements are carried out by sending the ac current through two distant diamond facets, and probing the voltage drop in between with a lock-in amplifier.

Specific heat measurements down to 0.7 K are performed by the ac-calorimetry technique. The basics of the method involve applying periodically modulated power and measuring the resulting temperature oscillations of the sample. In the proper frequency regime, the heat capacity of the sample is inversely proportional to the amplitude of the temperature oscillations. The experimental method and instrument are similar to the ones described in Ref. [17]. In our case, an optical fiber is used to guide the heating power from a light-emitting diode towards the sample. The temperature of the sample is recorded by the chromel-constantan thermocouple which had been calibrated from measurements on ultrapure silicon. Although our ac calorimeter is not capable of measuring the absolute values of the heat capacity, it is very sensitive for measurements of relative changes on minute samples such as our coarse diamond pieces with a volume smaller than 1 mm^3. To measure the heat capacity of our HPHT diamond, the two distant facets, through which ac current is sent for electrical transport measurements, are used for temperature sensing.

C. STM and STS experiments

After characterizing the bulk properties of the sample with electrical transport and heat capacity measurements, we look into its local superconductivity by performing STM and STS experiments. Atomically sharp STM tips are formed *in situ* by controlled collision of the Au tip with a clean Au surface at cryogenic temperatures [18]. We scan different surface areas in between the two distant facets of the sample. Surface topography is acquired in the constant current mode with a tunneling resistance of 500 kΩ. Zero bias conductance maps were acquired by the current imaging tunneling spectroscopy mode [19].

The tunneling conductance curves $G(V,x,y) = dI(V,x,y)/dV$ vs V are calculated by numerical differentiation of the locally measured I-V characteristics. Since the metallic Au tip features a constant density of states at the measured bias energies, each of the differential conductance vs voltage spectra reflects the local superconducting density of states (SDOS) of the sample, smeared by $\sim \pm 2k_BT$ in energy at the respective temperature. Consequently, in the low temperature limit, the differential conductance measures directly the SDOS.

III. RESULTS

Figure 1(a) shows the thermoresistivity $\rho(T)$ measured in the temperature range of 0.3 K–300 K at zero magnetic field. At 300 K, our samples have a normal-state resistivity one order of magnitude lower than that of diamonds

situated in the vicinity of the metal-insulator transition [8]. The $\rho(T)$ increases slightly when lowering temperature from the room temperature, and the resistive superconducting transition takes place at 4.89 K. The negative temperature coefficient of resistivity at normal state suggests that the heavily doped HPHT diamonds are dirty metallic, and granular disorder-correlated localization of charge carriers has a significant influence on the electrical transport at high temperatures. Similar observations were also ever made for granular disordered CVD diamond films [8–11].

The magnification of the superconducting transition of two HPHT diamonds is shown in the inset to Fig. 1(a). At first glance, the two samples HPHT1 and HPHT2 seem to have very different $\rho(T)$ behaviors, i.e., the resistive superconducting transition of HPHT1 demonstrates an anomalous peak while HPHT2 undergoes a two-step transition. It, however, turns out that entangled with the $\rho(T)$ peak, there is also a two-step superconducting transition in HPHT1 as revealed by our $\rho(T)$ measurements in magnetic fields [see Fig. 1(b)]. We tracked the transformation from the resistive superconducting transition, on which the $\rho(T)$ peak is superimposed, to the two-step transition in different magnetic fields. When increasing the magnetic field, the $\rho(T)$ peak diminishes in amplitude, shifts to a lower temperature, and turns into a bump. It is also noteworthy that along with the diminishing of the peak amplitude, the first-step superconducting transition, preceding the $\rho(T)$ peak, is resumed.

Consistent with the results of our thermoresistivity measurements, the anomalous resistance peak is also found when measuring the resistivity as a function of magnetic field $\rho(B)$. Figure 2(a) presents the $\rho(B)$ peak observed in the low field region, and Fig. 2(b) illustrates the 3D interpolation of the data.

The suppression and shift of the $\rho(T)$ peak in magnetic fields, and its entanglement with the superconducting transition, all suggest the presence of Cooper pairs at the abrupt $\rho(T)$ increase. To verify the bosonic nature of the anomalous $\rho(T)$ peak, we perform specific heat measurements on HPHT1 down to 0.7 K and up to 5 T. The temperature dependence of C/T in different magnetic fields is plotted in Fig. 3(a). Rather than an abrupt jump, the zero-field specific heat demonstrates a gradual increase below the onset temperature 4.89 K of the superconducting transition. Moreover, two specific heat peaks are found in sequence with their C/T maxima located at 4.05 and 2.76 K, respectively. The observation of these two broad C/T peaks suggests that the opening temperature of the superconducting gap (local critical temperature) in our system is strongly inhomogeneous, and the set of the local critical temperatures consists of two main subsets [20].

When increasing the magnetic field, both C/T peaks are suppressed and shifted to lower temperatures. The suppression of the second peak at 2.76 K is more pronounced than that of the first one at 4.05 K. Meanwhile, the left shoulder of the first peak overlaps more and more with the second peak during the shift, forming a single bump in

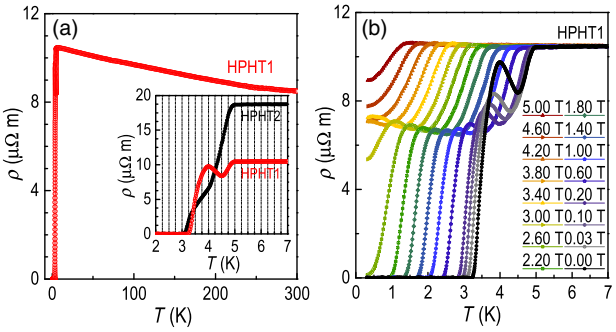

FIG. 1. The dirty metallic normal state and the resistive superconducting transition of heavily boron-doped polycrystalline diamonds synthesized with the high-pressure high-temperature (HPHT) method. (a) Despite the negative temperature coefficient of resistivity, the normal-state $\rho(T)$ increases when lowering temperature is far smaller than the criterion of $\Delta\rho|_{\text{per 10 K}} > 10\%$ for an insulating state, suggesting the dirty metallic normal state induced by weak disorder. Inset: sample HPHT2 exhibits a two-step superconducting transition, while sample HPHT1 demonstrates an anomalous $\rho(T)$ peak superimposed in its resistive superconducting transition. (b) In magnetic fields, the anomalous $\rho(T)$ peak of HPHT1 diminishes into a bump, leaving behind a two-step feature of the superconducting transition.

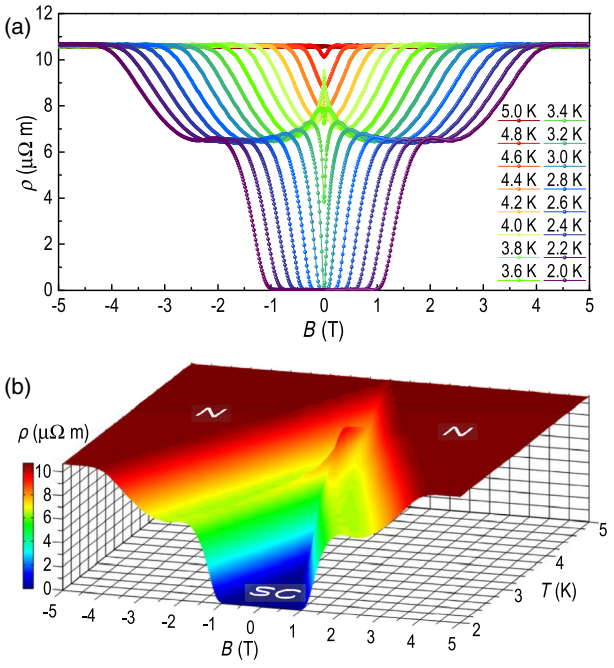

FIG. 2. The anomalous resistance peak observed when measuring the resistivity as a function of magnetic field $\rho(B)$. (a) Consistent with the $\rho(T)$ measurements, the anomalous resistance peak, situated in the low field regime, is suppressed and shifted in higher magnetic fields. (b) The 3D view of the interpolated data of (a).

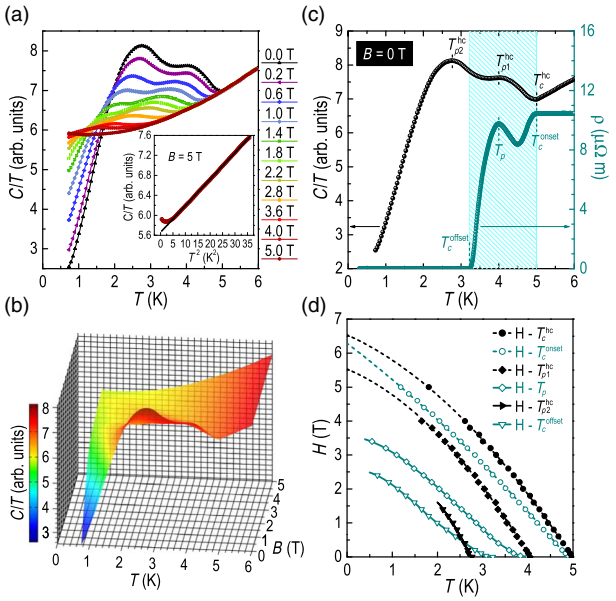

FIG. 3. Anomalous specific heat peaks found below the onset critical temperature of the superconducting transition. (a) The temperature dependence of specific heat over T, C/T. Rather than a single jump, two broad C/T peaks are observed for the polycrystalline bulk diamond. The behavior of the C/T peaks in magnetic fields is tracked up to 5 T. Inset: With the linear fitting of C/T ($B = 5$ T) vs T^2, we disclose that our HPHT diamond has a normal state of classic BCS superconductors. (b) The 3D view of the interpolated data of (a). (c) When plotting $\rho(T)$ and C/T together, the anomalous $\rho(T)$ peak is found to be within the temperature window of the C/T peak at T_{p1}^{hc}, and the other C/T peak is located at the tail of the resistive superconducting transition with its maximum temperature $T_{p2}^{\mathrm{hc}} < T_c^{\mathrm{offset}}$. The magnetic field dependence of the characteristic temperatures as determined in (c) is summarized in (d), yielding accordingly the phase boundaries.

higher magnetic fields and at lower temperatures. The inset to Fig. 3(a) displays the linear fit of C/T vs T^2 for $B = 5$ T (see the dashed black line). As shown by the fitting, the applied magnetic field of 5 T is not high enough to completely suppress the superconductivity at low temperatures and hence, the normal state is recovered only down to about 2 K. The linear behavior of C/T vs T^2 in the normal state indicates that our HPHT diamonds are conventional BCS superconductors with a Debye lattice following the law of $C/T = \gamma + \beta T^2$. Figure 3(b) provides the 3D interpolation of C/T as a function of T and B.

The bosonic anomalies, observed in the measurements of $\rho(T)$ and C/T, are plotted together in Fig. 3(c) for a detailed survey. Characteristic temperatures of $T_c{}^{\mathrm{hc}}$, T_{p1}^{hc}, and T_{p2}^{hc} are defined as the temperature where C/T starts increasing and where C/T reaches the local maxima, respectively. To characterize the resistive superconducting transition, $T_c{}^{\mathrm{onset}}$, T_p, and $T_c{}^{\mathrm{offset}}$ are defined as the temperature where ρ starts decreasing, where the $\rho(T)$ peak is located, and where ρ drops down to 0, respectively. The crossover of different phase boundaries as determined by the C/T and $\rho(T)$ measurements in magnetic fields can be seen in Fig. 3(d).

To gain further insight into the bosonic anomalies, we perform STM and STS measurements on HPHT1. Throughout a (500×500)-nm region [see Fig. 4(a)], the

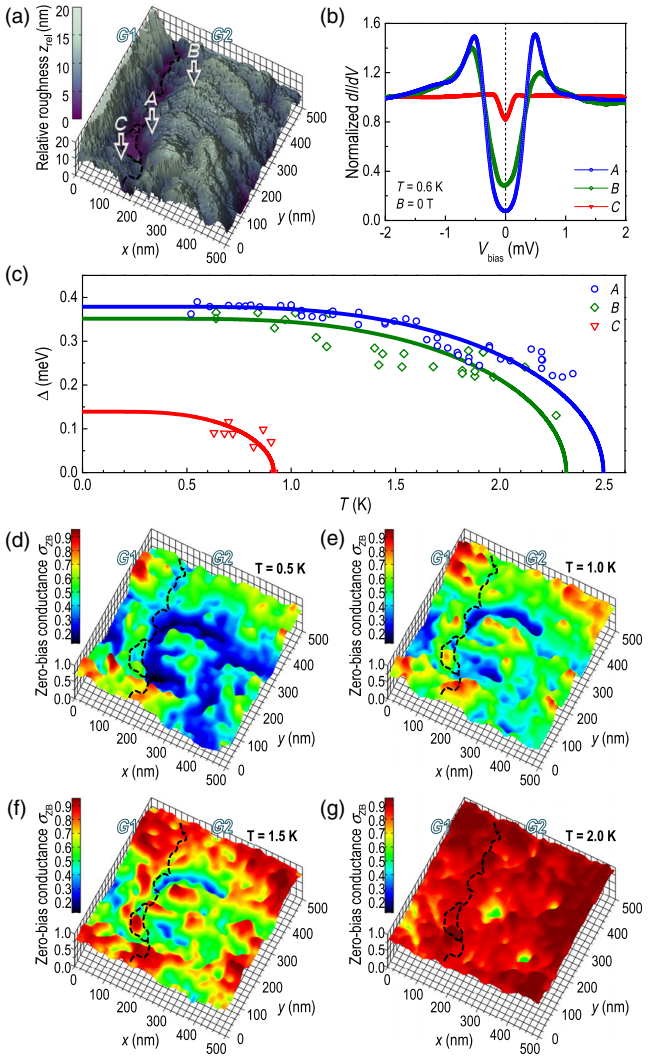

FIG. 4. Topography and temperature-induced evolution of the superconducting gap width and the zero-bias conductance (ZBC) map. (a) The topographic image of a (500×500)-nm-sized surface area, on which the grain boundary in between grain 1 ($G1$) and grain 2 ($G2$) is marked with dashed white lines. (b) The superconducting gap measured at three different locations labeled as A, B, and C in (a). (c) Temperature-induced evolution of the superconducting gap. The solid curves are the BCS fit to the half-width of the superconducting gap Δ (hollow symbols) at different location. (d)–(g) Temperature-induced evolution of the ZBC map, providing information about the depth variation of the superconducting gap. Intrinsic granularity is found to play a role in defining the modulations of Δ on a scale much smaller than the size of physical grains (extrinsic granularity).

differential conductance dI/dV spectra are collected and normalized to the dI/dV value far outside the superconducting gap [see Fig. 4(b), for instance]. Analysis of the dI/dV spectra provides us with information about both the width and depth of the superconducting gap. The superconducting gap 2Δ is obtained by fitting the Dynes formula to the measured spectra. The dense spatial variation of the SDOS intensifies the intrinsic noise of the experimental apparatus, resulting in broadened spectra with an unstable and uneven background. Hence, to fit our spectra, the Dynes modification of the thermally smeared BCS density of states is used [21]. Figure 4(c) shows the temperature-induced evolution of Δ at three different locations [see A, B, and C in Fig. 4(a)]. From the BCS fit to $\Delta(T)$, $T_c = 2.50$ K, 2.32 K, and 0.92 K, and $\Delta(0\ \mathrm{K}) = 0.38$ meV, 0.35 meV, and 0.14 meV are deduced for the locations of A, B, and C, respectively, yielding a universal value of $2\Delta(0\ \mathrm{K})/k_B T_c = 3.52$ at different locations. The substantial difference between the $\Delta(0\ \mathrm{K})$ and T_c values, obtained from the two different grains ($G1$ and $G2$), clearly indicates that our HPHT diamond is granular disordered. By taking the dI/dV values at zero-bias voltage [see the dashed line in Fig. 4(b)], we construct the zero-bias conductance σ_{ZB} maps. Figures 4(d)–4(g) display the temperature-induced evolution of σ_{ZB}. At $T = 0.5\ \mathrm{K} < T_c^{\mathrm{offset}}$, spatial variations of σ_{ZB} are already present in $G1$ and $G2$, and superconducting vales are found in $G2$. When increasing the temperature, the locally emerged normal states block the vales into superconducting lakes.

On the surface of HPHT1, we perform STM scans in multiple regions, while no superconducting gap is found above T_c^{offset} in any of the randomly chosen areas, prohibiting us from a detailed survey of the bosonic droplets at higher temperatures. Our STM and STS measurements, however, demonstrate the presence of the inhomogeneity of the local critical temperature in boron-doped granular diamond. On the other hand, more than a coincidence, the experimental fact of the absence of superconductivity in our scanned surface areas also suggests the percolation-based conduction and superconductivity mechanism of disordered diamond.

IV. DISCUSSION

Different from superconductors in the clean limit, boron-doped polycrystalline HPHT diamonds are both granularly and uniformly disordered. Despite the heavy boron doping of the diamond grains (intragrain substitutional boron concentration $n_{\mathrm{boron}} \sim 2.9 \times 10^{21}\ \mathrm{cm}^{-3}$ [7]), the grain boundaries, in which boron atoms are embedded as deep-level impurities, make the whole system a resistor network [11]. When taking into account the difference between the incorporation efficiency of boron dopants in the diamond grains with different crystalline orientations [22], this resistor network becomes even more complex and, thus, not only physical granularity in morphology (known as extrinsic granularity) but also electronic granularity due to chemical potential modulations (known as intrinsic granularity) play a role in defining the percolative conduction-superconductivity mechanism of the system. In our single crystalline diamond grains, structural imperfections such as inhomogeneous boron doping can result in chemical potential variations at sub-grain-size scales [23,24]. For superconductivity, the resistor network transforms into a superconductor-insulator-superconductor (S-I-S) junction network at low temperatures and according to the percolation threshold in 3D, only about 20% of the extrinsic and intrinsic grains need to be superconducting and coupled with each other via the S-I-S junctions. Since our HPHT diamonds are situated deep on the metallic side of the boron-doping-driven insulator-metal transition of diamond [8,25], it is highly likely that the proximity effect also contributes to the establishment of the percolation path, lowering the percolation threshold even further.

Based on the resistor network and S-I-S junction network, we interpret the bosonic anomalies of $\rho(T)$ and C/T as follows (see Fig. 5): above T_c^{onset} thermally activated single quasiparticles along the percolation path contribute to the electrical transport of the system [see Fig. 5(a)], resulting in the dirty metallic normal state (see Fig. 1). As the temperature decreases below T_c^{onset}, the superconducting gap starts to open. In the presence of weak disorder, the opening of the superconducting gap is spatially inhomogeneous, resulting in the formation of precursor bosonic droplets. Local phase locking sets in between some of these bosonic droplets [see Fig. 5(b)], leading to the initial decrease of $\rho(T)$ below T_c^{onset} (see Fig. 1). Note that the resistive superconducting transition is a process during which the bosonic channel takes over the control of electrical transport from the fermionic channel. In the presence of disorder, single quasiparticles are gradually removed from the fermionic channel to charge the bosonic channel by first forming isolated localized bosonic islands

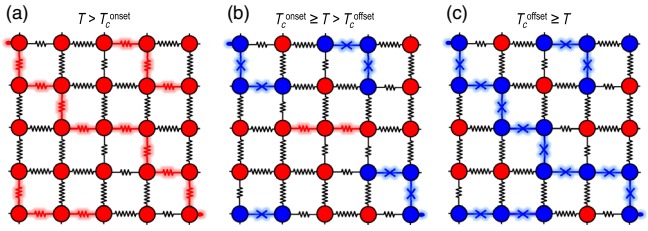

FIG. 5. The resistor–superconductor-insulator-superconductor (S-I-S) junction network model, based on which the bosonic $\rho(T)$ and C/T anomalies are interpreted. Note that the solid circles (red for normal state and blue for superconducting state) should be viewed as intrinsic and/or extrinsic grains. The percolation and condensation path is highlighted by glowing polylines. Blue crosses denote the S-I-S junctions. (a)–(c) illustrate the physics picture for normal-state, resistive superconducting transition, and superconducting state ($\rho = 0$) in the presence of intrinsic and extrinsic granularity-correlated disorder, respectively.

(groups of phase-locked bosonic droplets). The anomalous $\rho(T)$ increase occurs, since the efficient removal of single quasiparticles takes place before the establishment of a percolation path for the dissipationless flow of charged bosons. When lowering the temperature further, the preformed bosonic islands continue to grow, and more and more bosonic islands are developed and coupled. The global phase coherence sets in between these developed bosonic islands and the bosonic channel takes full control of electrical transport at $T \leq T_c^{\text{offset}}$ [see Fig. 5(c)] [16].

For the resistive superconducting transition in $\rho(T)|_{B\neq 0}$, the competition between the fermionic and bosonic channels is stimulated by the applied magnetic field. On one side, single quasiparticles, released from the preformed isolated bosonic droplets due to Cooper pair breaking, can charge the fermionic channel and delay the intervention of the bosonic channel. On the other hand, the released single quasiparticles can also charge the bosonic channel by forming new droplets when lowering the temperature, and thus contribute to the establishment of the percolation path for charged bosons.

We emphasize that in the physics picture described above, the emergence of the anomalous $\rho(T)$ peak is dependent not on the presence of the two-step superconducting transition but on the temperature difference between two scenarios, i.e., the extinction of single quasiparticles takes place before the global phase coherence. For instance, besides our HPHT2, there are also other systems in which a similar two-step resistive superconducting transition was present, while no anomalous $\rho(T)$ peak was observed [26,27]. On the other hand, there are also cases, including boron-doped CVD diamond films, in which an anomalous $\rho(T)$ peak preceding a single step transition was found [16,28–30]. In the framework of our model, disorder is considered as a crucial factor that delays the onset of the global phase coherence and thus triggers the temperature difference between the extinction of single quasiparticles and the global phase coherence. However, the degree of disorder, required for the emergence of the anomalous $\rho(T)$ peak, might not be too high, since otherwise the broad distribution of the local critical temperature would slow down the process of the extinction of single quasiparticles and overlap with the global phase-coherence temperature. This might be the reason why, so far, the anomalous $\rho(T)$ peak has been observed only in some systems with a relatively low normal-state resistivity [16,28–30]. The correlation between the anomalous resistivity increase and the normal-state resistivity was ever observed in some CVD diamond films [9,16]. Note that due to the accidental observations of the anomalous $\rho(T)$ peak in different systems, its origin still remains an open question. Our interpretation of this anomalous phenomenon, based on the influence of weak disorder (a possible common ground between different systems), may stimulate experimental and theoretical research in this field.

In the framework of our physics picture, we model the resistive superconducting transition in HPHT1 by considering three different cases, in which fermionic and bosonic channels are connected in parallel. In the first case, a fermionic channel with single quasiparticle resistivity ρ_N is connected in parallel to a bosonic channel with "superconducting" resistivity ρ_S [see Fig. 6(a)], giving rise to the total resistivity

$$\rho_{\text{total}} = \frac{\rho_N \rho_S}{\rho_N + \rho_S}, \tag{1}$$

where ρ_N is semiempirically modeled as

$$\rho_N = \rho_M - \left[2\int_{\Delta(T)}^{\infty} g(E) f'(E) dE\right]^{-1}, \tag{2}$$

and ρ_S is empirically written as

$$\rho_S = \rho_0 \left(\frac{T}{T_c^{\text{offset}}} - 1\right)^{\eta}. \tag{3}$$

ρ_M is the residual resistivity of the dirty metallic state, $g(E) = E/[E^2 - \Delta(T)^2]^{1/2}$ is the single quasiparticle

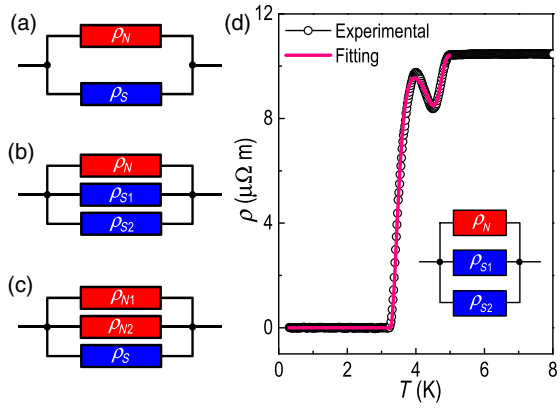

FIG. 6. Modeling of the anomalous resistive superconducting transition by using different multichannel circuits. Considering that a resistive superconducting transition is a process in which Cooper pairs take over the control of electrical transport from single quasiparticles, we borrow the switchlike function of parallel circuits for the development of three different models. (a) The two-channel model, composed of one fermionic channel ρ_N and one bosonic channel ρ_S, fails to describe our $\rho(T)$ peak superimposed in the two-step superconducting transition, although it can generally provide good fits to resistance peaks situated at the very onset of resistive superconducting transitions. (b) The three-channel model, composed of one fermionic channel ρ_N and two bosonic channels ρ_{S1} and ρ_{S2}, describes the anomalous resistive superconducting transition fairly well, as shown in (d). (c) The three-channel model, composed of two fermionic channels ρ_{N1} and ρ_{N2} and one bosonic channel ρ_S, ended up with a failure when fitting the resistive superconducting transition.

density of state in BCS theory, and $f'(E)$ is the derivative of the Fermi-Dirac distribution. Close to T_c^{onset}, $\Lambda = \Lambda_0(1\text{-}T/T_c^{\text{onset}})^{1/2}$ is taken as the parabolic approximation for $\Delta(T)$. ρ_0, η, and $\Lambda_0 = 1.74\Delta\,(0\text{ K})$ are left as fitting parameters. Note that the integral in the expression of ρ_N reflects the removal of single quasiparticles from the fermionic channel due to the Δ opening [16].

Although the two-channel model mentioned above can generally provide good fits to resistance peaks with different amplitude, it fails to describe our $\rho(T)$ peak which is entangled with the two-step superconducting transition. Above, we interpret the two-step superconducting transition as a result of two phase-coherence events one after the other, i.e., local phase locking between some preformed bosonic droplets sets in at a higher temperature and the global phase coherence sets in at a lower temperature due to the presence of disorder [26]. Accordingly, we modify the model by introducing one more bosonic channel into it [see Fig. 6(b)]:

$$\rho_{\text{total}} = \frac{\rho_N\rho_{S1}\rho_{S2}}{\rho_N\rho_{S1} + \rho_N\rho_{S2} + \rho_{S1}\rho_{S2}}, \tag{4}$$

where ρ_N remains the same as in Eq. (2), while

$$\rho_{S1} = \rho_{M1} + \rho_1\left(\frac{T}{T_d} - 1\right)^{\chi} \tag{5}$$

is taken as an empirical expression for the first-step superconducting transition (local phase coherence at higher temperature) preceding the anomalous resistance increase, and

$$\rho_{S2} = \rho_S = \rho_0\left(\frac{T}{T_c^{\text{offset}}} - 1\right)^{\eta} \tag{6}$$

for the second-step superconducting transition (global phase coherence at lower temperature). The experimental values of $T_c^{\text{onset}} = 5$ K, $T_c^{\text{offset}} = 3.2$ K, $T_d = 4.4$ K (where the resistance dip is located), and $\rho_M = 10.43\ \mu\Omega\,\text{m}$ were used for the fitting. As shown in Fig. 6(d), the three-channel model, composed of two bosonic channels and one fermionic channel, reproduces fairly well the observed anomalous superconducting transition, and $\Lambda_0 = 1.65$ meV, $\rho_{M1} = 16.5\ \mu\Omega\,\text{m}$, $\rho_1 = 79\,\text{k}\Omega\,\text{m}$, $\chi = 3.8$, $\rho_0 = 1.95\ \text{k}\Omega\,\text{m}$, and $\eta = 2.11$ were obtained as fitting parameters. Despite our limited knowledge of the physics meaning of the ρ_{M1}, ρ_1, χ, ρ_0, and η values, we emphasize that $\Lambda_0 = 1.65$ meV yields a $2\Delta(0\text{ K})/k_BT_c$ value of 4.4, which deviates not much from our STM and STS measurement result of $2\Delta(0\text{ K})/k_BT_c = 3.52$.

In the case of three channels connected in parallel, we also look into the possibility of modeling the resistive superconducting transition by introducing an additional fermionic channel into Eq. (1) rather than a bosonic one as in Eq. (4) [see Fig. 6(c)], i.e.,

$$\rho_{\text{total}} = \frac{\rho_{N1}\rho_{N2}\rho_S}{\rho_{N1}\rho_{N2} + \rho_{N1}\rho_S + \rho_{N2}\rho_S}, \tag{7}$$

where ρ_S remains the same as in Eq. (3), while

$$\rho_{N1} = \rho_N = \rho_M - \left[2\int_{\Delta(T)}^{\infty} g(E)f'(E)dE\right]^{-1} \tag{8}$$

is taken as a semiempirical description for the removal of single quasiparticles from channel $N1$ due to the opening of Δ below $T_c^{\text{onset}} = 5$ K, and

$$\rho_{N2} = \rho_m - \left[2\int_{\delta(T)}^{\infty} G(E)f'(E)dE\right]^{-1} \tag{9}$$

for the removal of single quasiparticles from channel $N2$ due to the opening of a second superconducting gap $\delta(T)$ below $T_d = 4.4$ K. In this case, $\delta_0(1\text{-}T/T_d)^{1/2}$ is taken as the parabolic approximation for $\delta(T)$ in the vicinity of T_d, and $G(E) = E/[E^2 - \delta(T)^2]^{1/2}$. In the framework of this model, although $\delta_0 \gg \Delta_0$ could give rise to the abrupt $\rho(T)$ increase below T_d, Eq. (7) failed to describe the entire resistive superconducting transition due to discontinuity at T_d.

The model which we use for describing the resistive superconducting transition can be directly applied to explain the C/T anomaly. As shown by the shadowed region in Fig. 3(c), the resistive superconducting transition mainly takes place within the temperature range where the first C/T peak is situated, and the resistivity drops down to 0 in the temperature window of the second C/T peak. As such, the C/T peak at T_{p1}^{hc} is considered to be responsible for charging the bosonic channel by forming bosonic islands [see Fig. 5(b)], while the C/T peak at T_{p2}^{hc} takes part in finalizing the bosonic percolation path by connecting up the bosonic islands [see Fig. 5(c)].

V. CONCLUSION

In heavily boron-doped polycrystalline diamond, we observe an anomalous $\rho(T)$ peak superimposed in the resistive superconducting transition and two broad C/T peaks below the onset critical temperature. Based on the resistor network model, the bosonic $\rho(T)$ and C/T anomalies are interpreted as a result of the quantum confinement and coherence effects of inhomogeneous superconductivity in the presence of disorder. We develop a three-channel model (two bosonic channels connected in parallel with one fermionic channel) for the modeling of the anomalous $\rho(T)$ peak. The inhomogeneity of superconductivity is confirmed by mapping the Δ modulations in a temperature-induced evolution with STM and STS. Our data, obtained from heavily doped granular diamond, clearly demonstrate that contrary to popular belief, even deep on the metallic side of the boron-doping-driven insulator-metal transition

of diamond weak disorder can still result in strong quantum confinement effects and thus anomalous physical properties. Moreover, our combined STM and STS, electrical transport, and specific heat data also justify the argument that the superconductivity in boron-doped granular diamond is based on percolation.

Our progress in diamond material science can be of practical concerns, when diamond-based devices such as micro- or nanodiamond SQUID and diamond-made local probing tips are discussed, since in many cases granular diamond rather than single crystalline diamond will be used to reduce the manufacturing costs, and then the influence of granular disorder on the device can hardly be neglected. On the other hand, instead of bringing a negative influence to diamond-based Josephson junction devices, the self-established grain boundary junctions may be directly borrowed for relevant device development. Furthermore, owing to the common grounds between HPHT and CVD diamonds, our research results, obtained from HPHT diamond, also shed light on the physical properties of CVD diamond films, which are considered as a promising candidate to be integrated into the well-developed silicon-based electronics.

ACKNOWLEDGMENTS

The work at KU Leuven was supported by the Methusalem Funding by the Flemish Government, the FWO projects, and the MP1201 COST Action. G. Z. acknowledges support from the FWO for a postdoctoral grant. T. S., J. K., and P. S. have been supported by APVV-0036-11, APVV-14-0605, VEGA 1/0409/15, VEGA 2/0149/16 and EU ERDF-ITMS 26220120005. E. A. E. is grateful for the support from the Russian Foundation for Basic Research under Grant No. 15-02-05603.

G. Z., T. S., and J. K. contributed equally to this work.

[1] P. W. May, Diamond thin films: A 21st-century material, Phil. Trans. R. Soc. A **358**, 473 (2000).

[2] E. A. Ekimov, V. A. Sidorov, E. D. Bauer, N. N. Mel'nik, N. J. Curro, J. D. Thompson, and S. M. Stishov, Superconductivity in diamond, Nature (London) **428**, 542 (2004).

[3] Y. Takano, M. Nagao, I. Sakaguchi, M. Tachiki, T. Hatano, K. Kobayashi, H. Umezawa, and H. Kawarada, Superconductivity in diamond thin films well above liquid helium temperature, Appl. Phys. Lett. **85**, 2851 (2004).

[4] S. Mandal, T. Bautze, O. A. Williams, C. Naud, E. Bustarret, F. Omnès, P. Rodière, T. Meunier, C. Bäuerle, and L. Saminadayar, The diamond superconducting quantum interference device, ACS Nano **5**, 7144 (2011).

[5] T. Hantschel, C. Demeulemeester, P. Eyben, V. Schulz, O. Richard, H. Bender, and W. Vandervorst, Conductive diamond tips with sub-nanometer electrical resolution for characterization of nanoelectronics device structures, Phys. Status Solidi A **206**, 2077 (2009).

[6] G. Zhang, J. Vanacken, J. Van de Vondel, W. Decelle, J. Fritzsche, V. V. Moshchalkov, B. L. Willems, S. D. Janssens, K. Haenen, and P. Wagner, Magnetic field-driven superconductor–insulator transition in boron-doped nanocrystalline chemical vapor deposition diamond, J. Appl. Phys. **108**, 013904 (2010).

[7] G. Zhang, S. Turner, E. A. Ekimov, J. Vanacken, M. Timmermans, T. Samuely, V. A. Sidorov, S. M. Stishov, Y. Lu, B. Deloof, B. Goderis, G. Van Tendeloo, J. Van de Vondel, and V. V. Moshchalkov, Global and local superconductivity in boron-doped granular diamond, Adv. Mater. **26**, 2034 (2014).

[8] T. Klein, P. Achatz, J. Kacmarcik, C. Marcenat, F. Gustafsson, J. Marcus, E. Bustarret, J. Pernot, F. Omnes, Bo E. Sernelius, C. Persson, A. Ferreira da Silva, and C. Cytermann, Metal-insulator transition and superconductivity in boron-doped diamond, Phys. Rev. B **75**, 165313 (2007).

[9] P. Achatz, W. Gajewski, E. Bustarret, C. Marcenat, R. Piquerel, C. Chapelier, T. Dubouchet, O. A. Williams, K. Haenen, J. A. Garrido, and M. Stutzmann, Low-temperature transport in highly boron-doped nanocrystalline diamond, Phys. Rev. B **79**, 201203(R) (2009).

[10] B. L. Willems, G. Zhang, J. Vanacken, V. V. Moshchalkov, S. D. Janssens, K. Haenen, and P. Wagner, Granular superconductivity in metallic and insulating nanocrystalline boron-doped diamond thin films, J. Phys. D **43**, 374019 (2010).

[11] G. Zhang, S. Janssens, J. Vanacken, M. Timmermans, J. Vacík, G. W. Ataklti, W. Decelle, W. Gillijns, B. Goderis, K. Haenen, P. Wagner, and V. V. Moshchalkov, Role of grain size in superconducting boron-doped nanocrystalline diamond thin films grown by CVD, Phys. Rev. B **84**, 214517 (2011).

[12] W. Gajewski, P. Achatz, O. A. Williams, K. Haenen, E. Bustarret, M. Stutzmann, and J. A. Garrido, Electronic and optical properties of boron-doped nanocrystalline diamond films, Phys. Rev. B **79**, 045206 (2009).

[13] F. Dahlem, P. Achatz, O. A. Williams, D. Araujo, E. Bustarret, and H. Courtois, Spatially correlated microstructure and superconductivity in polycrystalline boron-doped diamond, Phys. Rev. B **82**, 033306 (2010).

[14] G. Zhang, Ph.D. thesis, Arenberg Doctoral School, 2013.

[15] E. Bustarret, Superconductivity in doped semiconductors, Physica (Amsterdam) **514C**, 36 (2015).

[16] G. Zhang, M. Zeleznik, J. Vanacken, P. W. May, and V. V. Moshchalkov, Metal–Bosonic Insulator–Superconductor Transition in Boron-Doped Granular Diamond, Phys. Rev. Lett. **110**, 077001 (2013).

[17] P. F. Sullivan and G. Seidel, Steady-state, ac-temperature calorimetry, Phys. Rev. **173**, 679 (1968).

[18] T. Samuely, P. Szabó, V. Komanický, J. G. Rodrigo, S. Vieira, and P. Samuely, Enhanced superconductivity in nano-sized tips of scanning tunneling microscope, Acta Phys. Pol. A **118**, 1038 (2010).

[19] R. J. Hamers, R. M. Tromp, and J. E. Demuth, Surface Electronic Structure of Si(111)-(7 × 7) Resolved in Real Space, Phys. Rev. Lett. **56**, 1972 (1986).

[20] V. A. Sidorov, E. A. Ekimov, S. M. Stishov, E. D. Bauer, and J. D. Thompson, Superconducting and normal-state

properties of heavily hole-doped diamond, Phys. Rev. B **71**, 060502(R) (2005).

[21] R. C. Dynes, V. Narayanamurti, and J. P. Garno, Direct Measurement of Quasiparticle-Lifetime Broadening in a Strong-Coupled Superconductor, Phys. Rev. Lett. **41**, 1509 (1978).

[22] E. Bustarret, Superconducting diamond: An introduction, Phys. Status Solidi (a) **205**, 997 (2008).

[23] M. Salluzzo, F. Palomba, G. Pica, A. Andreone, I. Maggio-Aprile, Ø. Fischer, C. Cantoni, and D. P. Norton, Role of Nd/Ba Disorder on the Penetration Depth of $Nd_{1+x}Ba_{2-x}Cu_3O_{7-\delta}$ Thin Films, Phys. Rev. Lett. **85**, 1116 (2000).

[24] A. I. Buzdin, V. N. Men'shov, and V. V. Tugushev, Localized states on defects in electronic transitions into a soliton-lattice state, Zh. Eksp. Teor. Fiz. **91**, 2204 (1986) [Sov. Phys. JETP **64**, 1310 (1986)].

[25] E. Bustarret, J. Kačmarčik, C. Marcenat, E. Gheeraert, C. Cytermann, J. Marcus, and T. Klein, Dependence of the Superconducting Transition Temperature on the Doping Level in Single-Crystalline Diamond Films, Phys. Rev. Lett. **93**, 237005 (2004).

[26] S. Eley, S. Gopalakrishnan, P. M. Goldbart, and N. Mason, Approaching zero-temperature metallic states in mesoscopic superconductor–normal–superconductor arrays, Nat. Phys. **8**, 59 (2011).

[27] I. Felner, E. Galstyan, B. Lorenz, D. Cao, Y. S. Wang, Y. Y. Xue, and C. W. Chu, Magnetoresistance hysteresis and critical current density in granular $RuSr_2Gd_{2-x}Ce_xCu_2O_{10-\delta}$, Phys. Rev. B **67**, 134506 (2003).

[28] M. A. Crusellas, J. Fontcuberta, and S. Piñol, Giant resistive peak close to the superconducting transition in $L_{2-x}Ce_xCuO_4$ single crystals, Phys. Rev. B **46**, 14089 (1992).

[29] M. Suzuki, Resistance peak at the resistive transition in high-T_c superconductors, Phys. Rev. B **50**, 6360 (1994).

[30] V. V. Moshchalkov, L. Gielen, G. Neuttiens, C. Van Haesendonck, and Y. Bruynseraede, Intrinsic resistance fluctuations in mesoscopic superconducting wires, Phys. Rev. B **49**, 15412 (1994).